Adsorption characteristics of Pb(II) onto magnetic GO-hydroxyapatite and the contribution of GO to its acid resistance

Ruifeng Li[a], Yongqiang Liu[b], Guihong Lan[a], Haiyan Qiu[a], Bo Xu[a,*], Qianxia Xu[c], Ningyan Sun[a], Lihui Zhang[a]

* Corresponding author

Email address: boxu416@sina.com (Bo Xu)

[a] *College of Chemistry and Chemical Engineering, Southwest Petroleum University (SWPU), Chengdu, 610500, China*

[b] *Faculty of Engineering and Physical Sciences, University of Southampton, Southampton SO17 1BJ, UK*

[c] *Sichuan Institute of Ecological and Environmental Science, Chengdu, 610041, China*

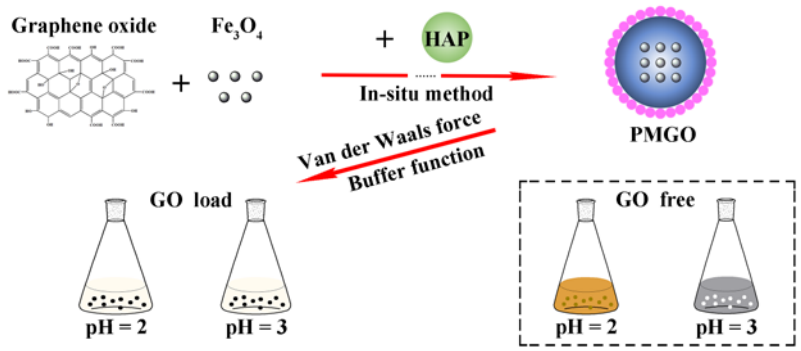

GRAPHICAL ABSTRACT

Abstract

Fe_3O_4, the functional component of magnetic adsorbent for separation, dissolves readily under acidic conditions, which significantly restricts its application for treatment of acidic wastewater such as acid mine drainage. Thus improving the acid resistance of Fe_3O_4 can expand the application domain of Fe_3O_4 as absorbents. This study developed a novel method to improve the acid resistance of Fe_3O_4 by doping it with graphene oxide (GO). Specifically, a novel absorbent material, i.e. magnetic GO-hydroxyapatite (PMGO), was synthesized by Fe_3O_4, GO, and hydroxyapatite (HAP). The effects of GO load in the magnetic hydroxyapatite (MP) material on the adsorption capacity and dissolution behavior of synthesized absorbents (MP without GO and PMGO with GO)at acidic and neutral conditions with pH from 1 to 8 were investigated. In addition, synthesized materials were characterized to explore their improved adsorption mechanism under acidic conditions. . It is found that the increase in GO amount in PMGO reduced the pore size from 21.10 (MP) to 0.41nm (PMGO) due to the distinct inhibition of self-polymerization of PMGO by GO, leading to the increase in the specific surface area of absorbent from 84.21 (MP) to 158.72 m^2/g (PMGO). Therefore, the adsorption capacity of PMGO for Pb(II) removal increased from 178.40 to 274.73 mg/g. At pH of 2.06, MP dissolved? MP is tough to recycle, while PMGO still maintained 90.10% magnetism, suggesting that the addition of GO into MP reduced its dissolution under acidic conditions. Moreover, , PMGO after 5 cycles of reuse still possessed 97.49 mg/g adsorption

capacity. This study developed a GO doped magnetic absorbent with significantly improved acid resistance, allowing magnetic adsorbent to be applied under acidic conditions. The findings have promising application in lead mine industry for lead ion removal from acidic mining wastewater.

Keywords: Acid resistance, Adsorption, Magnetic, Graphene oxide, Hydroxyapatite

1. Introduction

Lead mining is conducted worldwide. It was reported that there are almost 240 active mines active but most of them have been abandoned for decades (Zhan et al., 2019). Abandoned Pb mines have potential environmental risks because they can form acid mine drainage (AMD), which contains high concentration Pb^{2+} and has low pH such as lower than 4 (Vélez-Pérez et al., 2020). As a harmful heavy metal, Pb can cause anemia, irritability, dizziness and renal sickness (Bagbi et al., 2016). Thus, removing Pb^{2+} from acid mine drainage before it is discharged to the environment is critical to protect public health and ecosystem.

Due to the excellent physicochemical properties, nanomaterials have currently attracted extensive attention in the fields of electrocatalysis (Ahsan et al., 2021), photocatalysis (Xiong et al., 2020), cancer (Sanad et al., 2019) and water treatment (Akın Sahbaz et al., 2018). Through preparing nanometer-sized Fe_3O_4, nanomaterials possess magnetism, which could be

recycled easily by an external magnetic field (Thanh et al., 2018). Fe_3O_4, however, easily dissolves under acidic conditions, resulting in its inapplicability to acidic solutions. Recently, it was reported that coating SiO_2 onto the Fe_3O_4 surface reduced the dissolution of Fe_3O_4 under acidic conditions (Sun et al., 2016), allowing magnetic materials to be used for the treatment of AMD for Pb^{2+} removal. However, SiO_2 tends to agglomerate during synthesis. In addition, due to its limited functional groups, there is no much room to further improve the property of SiO_2 coated magnetic materials h. Developing a new acid resistant magnetic material with more functional groups and less agglomeration propensity is imperative.

Graphene oxide (GO) has been reported to have more uniform dispersion in the synthetic magnetic materials (Fang et al., 2016). Furthermore, it is able to inhibit the self-polymerization of Fe_3O_4 (Pudukudy et al., 2019). Thus, it has a broad application prospect in the field of magnetic materials. Currently, in-situ method has been widely used in synthesizing magnetic graphene oxide (MGO) (Szymczyk et al., 2019). It is believed that -OH and -COOH groups of GO could bind with Fe_3O_4 , and thus reduce the release of Fe^{3+} under acidic conditions. Furthermore, $-COO^-$ on GO surface (Guo et al., 2016) could play a buffer role to against the dissolution of Fe_3O_4 under acidic conditions. To the authors' knowledge, although there is some research work on MGO for water treatment, if GO can inhibit the dissolution of Fe_3O_4 under acidic conditions hasn't been reported. If this proves to be effective, the potential of GO to

enhance the acid resistance of Fe_3O_4 will allow a broader application of magnetic materials particularly under acidic solutions. .

Therefore, this study aimed to develop a novel method to dope Fe_3O_4 with GO to improves both the acid resistance and the functionality of magnetic materials. To allow this GO doped Fe_3O_4 materials for Pb^{2+} adsorption, hydroxyapatite (HAP) was selected in this study due to its excellent adsorption capacity for Pb^{2+} (Fan et al., 2019) to modify the property of GO doped Fe_3O_4 materials. Based on this, the newly synthesized MPGO materials were characterized to understand its adsorption mechanisms and evaluated for its adsorption capacity and reuse under acidic conditions for Pb^{2+} removal. The study can make a contribution to the development of new magnetic adsorbent for Pb^{2+} removal from acid wastewater. .

2. Materials and methods

2.1. Chemicals

Graphite powder was purchased from Shenzhen Turing Evolution Technology (Shenzhen, China), while $FeCl_3$, $FeSO_4 \cdot 7H_2O$ and other chemicals were purchased from Kelong Chemical (Chengdu, China). All reagents used were analytical grade, and water used was Deionized (DI) water.

2.2. Preparation of Materials

GO was prepared from graphite powder using the *freeze-drying* method reported by

Hummer's (Hou et al., 2020). Fe_3O_4 was prepared by co-precipitation method (Panella et al., 2009), by which Fe^{3+} and Fe^{2+} with 2:1 molar ratio was mixed in aqueous ammonia solution. MP was prepared by in-situ method according to (Thanh et al., 2018). by which Fe_3O_4 and HAP were mixed in a molar (??) ratio of 1:4. MGO was prepared by using a previously reported co-precipitation method (Luo et al., 2018). PMGO was also prepared by in-situ method, the dosage of GO was controlled at 0.1 g - 1.0 g. Its preparation process is followed in Table S1 and the schematic diagram is shown in **Figure 1**.

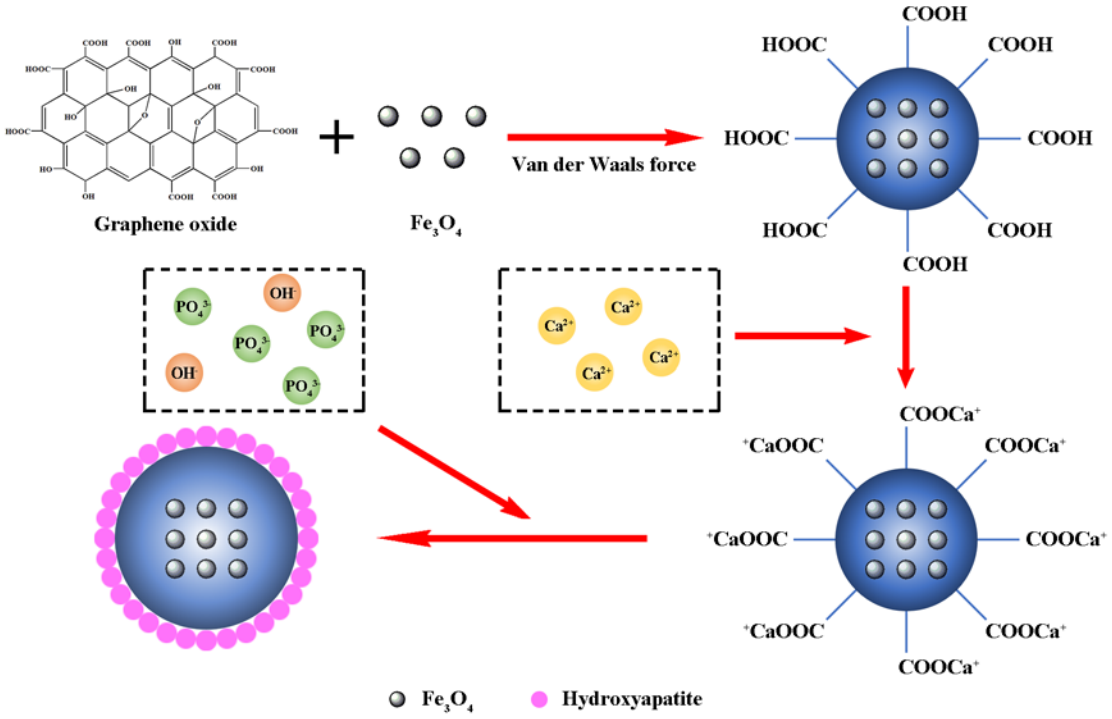

Figure 1. Schematic diagram for the preparation of PMGO**.**

To compare the materials, the synthesis of materials were carried out under the same conditions and dosage proportions, and the resulting suspensions were washed, dried and ground into powder for standby application.

2.3. Characterization of synthesized materials

The morphology and size of synthesized materials were analyzed by using scanning election microscopy (SEM, JSM7500F, JEOL, Japan). An energy dispersive X-ray spectroscopy (EDS, X-Max 50, Oxford Instruments, UK) equipped with SEM was performed to analyze the elemental composition of materials. X-ray photoelectron spectroscopy (XPS, EscaLab 250XI, Thermo Scientific, US) was utilized to study the valence electron structure. A DXR Smart Raman (Raman, LabRAM HR Evolution, Horiba Scientific, France) was used to investigate the interaction of bonds.

The structure of materials was characterized by X-ray powder diffraction (XRD, X'Pert PRO, PANalytical, Netherlands). Thermogravimetric analysis (TGA, SDTA851e, METTLER TOLEDO, Switzerland) was used to investigate the thermal stability in oxygen-free environment. The specific surface area was determined by Brunauer-Elmet-Teller nitrogen adsorption (BET-N_2 adsorption, ASAP2460, Micromeritics, US) technique method. Vibrating Sample Magnetometer (VSM, PPMS-9, Quantum Design, US) was used to evaluate magnetism.

2.4. Pb^{2+} adsorption by synthesized MP and PMGO materials

PMGO (10 - 150 mg) was dispersed into 50 mL solution with 300 mg/L Pb^{2+} at 180 rpm for 3 h. pH from 1 to8), adsorption duration from 5 to 4320 min, concentrations from 200 to 800 mg/L and temperature from 15 to35 ℃ were studied under the condition with 50 mg PMGO

and 50 mL Pb^{2+} solution at 180 rpm.

To investigate the interference of other metal ions such as Na+, K+, Ca2+, Mg2+, Fe3+ on Pb^{2+} adsorption by PMGO, $NaNO_3$, KNO_3, $Ca(NO_3)_2$, $Mg(NO_3)_2$, $Fe(NO_3)_3$ with concentrations from 0.01 to 0.1 M were prepared for adsorption with Pb^{2+},studied, respectively.). Different chemicals were used to study the reusability of PMGO. In all adsorption experiments by MPGO, MP used as the control to compare the efficacy of addition of GO for improved adsorption under acidic conditions. . Meanwhile, blank control was used to eradicate the influence of the non-human factors.Residual Pb^{2+} concentrations after adsorption were measured by atomic absorption spectrophotometer (AAS, SP-3520AA, Spectrum Instruments, China). To minimize, . All data presented in this study was the average of triplicate experiments. 2016.

2.5. Calculation

Adsorption capacity (mg/g) of the adsorbents was calculated by using the following equation (Bagbi et al., 2016):

$$Q_e = \frac{(C_0 - C_e) \times V}{m} \quad (1)$$

Where Q_e is the adsorption capacity (mg/g.); C_0 and C_e are the initial and equilibrium Pb^{2+} concentrations (mg/L.); V is the Pb^{2+} solution volume (L.); m is the dose of adsorbents (g.).

The role of ion exchange is expressed by the following formula (Thanh et al., 2018):

$$Ca_E = nCa_R^{2+} - nCa_B^{2+} = \frac{C_E \cdot V}{M} - \frac{C_B \cdot V}{M} \quad (2)$$

$$\eta = \frac{Ca_E \cdot M_{Pb}}{m_e} \cdot 100\% \quad (3)$$

Where Ca_E is the mole of Ca^{2+} in ion exchange (mol.); nCa_R^{2+} and nCa_B^{2+} are the moles of released Ca^{2+} in the experiment and blank sample (mol.); C_E and C_B are the concentration of released Ca^{2+} in experiment and blank sample (g/L.); V is the solution volume (L.); M and M_{Pb} are the atomic weight of Ca and Pb (g/mol.); η is the role of ion exchange in adsorption; m_e is the adsorbed Pb^{2+} mass of PMGO per unit mass (g.).

Moreover, this study employed the pseudo first-order kinetic, pseudo second-order kinetic and intra-particle diffusion models to understand the adsorption process (Esfandiari et al., 2020), Langmuir and Freundlich models were used to comprehend the adsorption mechanism (Ahsan et al., 2020a), the thermodynamic parameters were calculated by using the Van't hoff equation (Islam et al., 2018). The corresponding equations were provided in the Supplementary material.

3. Results and discussion

3.1. Characterization of materials

3.1.1. Morphological Characteristic of materials by SEM

Morphologies of MP, PMGO-a (before adsorption) and PMGO-b (after adsorption) observed under SEM were shown in Figure S1, suggesting nanoscale of these materials. It can be seen that graphene layer in GO increased the vertical dimension (~ 120 nm to ~ 150 nm),

157 uniformity and dispersity of PMGO. Nanoscale and ideal dispersity can provide more
158 adsorption sites for Pb^{2+}, thus improving the adsorption capacity of PMGO. Pb^{2+} adsorption led
159 the increase in the vertical dimension (~ 150 nm to ~ 180 nm) of PMGO analogously, which
160 makes the energy of nanomaterials more stable and tends toward agglomeration, so Pb^{2+} is
161 adsorbed successfully on PMGO.

162 3.1.2. Elemental Composition of materials analyzed by EDS andXPS)

163 Table S2 shows the elemental contents of MP, PMGO-a and PMGO-b. It can be seen that
164 the relative content of C increased from 5.64% in GO to 16.55% in PMGO, Furthermore, it is
165 noted that after Pb^{2+} adsorption, the relative content of Ca in PMGO decreased while Pb
166 increased , indicating ion exchange between Ca and Pb in Pb^{2+} adsorption (Thanh et al., 2018).

167 As shown in **Figure 2a**, elements C, O, Ca, Fe and P in PMGO were detected by EDS, and
168 the successful synthesis of PMGO was verified by XPS. Characteristic signals of C1s (**Figure**
169 **2b**) were recognized as C-C (284.8 eV), C-O (286.4 eV) and C=O bonds (288.4 eV) in GO
170 (Pudukudy et al., 2019), while O1s (**Figure 2c**) peaks were ascribed to Fe_3O_4 (530.0 eV), C=O
171 (531.5 eV) and C-O (532.8 eV) bonds (Guo et al., 2016). Moreover, Ca2p (**Figure 2d**, 347.6
172 eV, 351.2 eV) and P2p (**Figure 2e**, 133.1 eV, 133.8 eV) peaks (López et al., 2019; Lovón-
173 Quintana et al., 2017) verified the presence of HAP in PMGO. **Figure 2f** shows the scan
174 spectra of Fe2p (724.8 eV, 718.7 eV, 712.4 eV, 710.7 eV), indicating the presence of Fe_3O_4 in

PMGO (Xu et al., 2019).

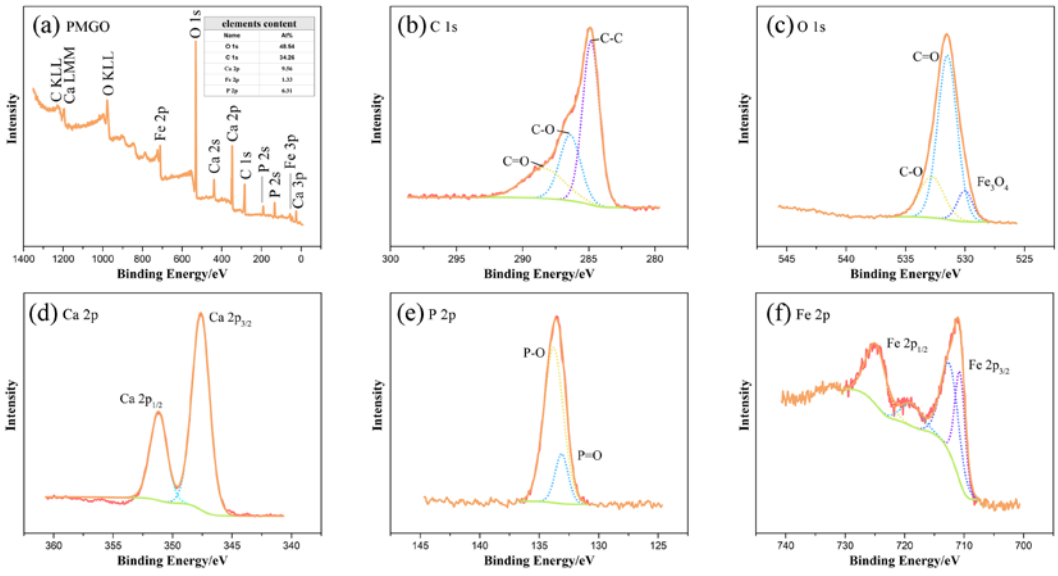

Figure 2. XPS spectrum of PMGO (**a** represents the total elemental peak, **b**, **c**, **d**, **e** and **f** represent the elemental peaks of C, O, Ca, P and Fe, respectively).

3.1.3. Chemical Properties of materials analyzed by FTIR and Raman

FTIR spectrum can reflect the functional groups of materials. Figure S2 shows FTIR results. Materials of Fe_3O_4, MGO, MP, PMGO and PMGO-b all showed the vibration peaks of Fe_3O_4 at 580 cm^{-1} (Cui et al., 2015). Meanwhile, abundant functional groups of GO provided active sites for the adsorption of Pb^{2+} by PMGO. 3378 (-OH), 1720 (C=O), 1587 ($-COO^-$) and 1047 (C-O-C) cm^{-1} were observed in GO loaded materials (Guo et al., 2016). Notably, sulfate peaks in GO were detected at 576 and 1176 cm^{-1} (Talla and Wildner, 2019), which proved to be $MnSO_4$ by XRD analysis. Wen et al. (???) synthesized a kind of graphene oxide-hydroxyapatite, HAP peaks were observed at 1037, 1452 and 1720 cm^{-1}, and the GO addition didn't apparently affect HAP peaks by FTIR (Wen et al., 2014). This phenomenon is consistent

189 with the peaks of PMGO observed in this study. Compared with PMGO and PMGO-b, the
190 peaks of PMGO were almost unchanged after adsorption, implying favorable potential for
191 material recycling.

192 Figure S3 shows the Raman spectra of GO and PMGO. D and G bands (1359 cm^{-1}, 1597
193 cm^{-1}) are two well-known peaks of GO. D band can be attributed to A_1g symmetry while G
194 band can be ascribed to the sp^2 carbon atoms (Ahsan et al., 2019). It was reported that four
195 vibrational modes e.g. 219 cm^{-1}, 283 cm^{-1}, 400 cm^{-1} and 698 cm^{-1} (Gupta et al., 2002) were
196 associated with Fe_3O_4 while three vibrational modes e.g. 599 cm^{-1}, 954 cm^{-1}, 1050 cm^{-1} (Ulian
197 and Valdre, 2018) were associated with HAP. Vibrational modes above indicate that Fe_3O_4 and
198 HAP still maintain their interactions of bonds after synthesis with their original functions. In
199 addition, it is noted that the intensity ratio of D to G bands (I_D/I_G) increased from 1.02 (GO) to
200 1.68 (PMGO), suggesting that the synthesis of PMGO caused the increased disorders and
201 defects inGO matrix (Ferrari, 2007).

202 3.1.4. Material characterization by XRD, BET, TGA, and VSM

203 XRD spectra of materials GO, Fe_3O_4, MGO, MP, PMGO and PMGO-b are shown in
204 **Figure 3a** and **Figure 3b**. An obvious signal of GO at 9.19° was observed (Beygmohammdi et
205 al., 2020), but meanwhile a weak $MnSO_4$ peak was noticed. This is probably from the reaction
206 between $KMnO_4$ and H_2SO_4 as these two chemicals were added as oxidizing agents in

Hummer's method for GO preparation .. The peaks of Fe_3O_4 and HAP observed in corresponding spectrograms indicate Fe_3O_4 and HAP were successfully synthesized in the MPGO materials (Lu et al., 2000; Thanh et al., 2018; Zhang et al., 2019). The disappearance of the original peaks of GO is likely eue to the disruption of monolayer structure of GO during the ultrasound process, (Ahsan et al., 2019). Notably, the peaks of PMGO-b, especially the Fe_3O_4 peaks, were markedly decreased after the Pb2+ adsorption, while the similar reduction of HAP peaks is probably due to the adsorption of Pb2+ by HAP in PMGO (Yusoff et al., 2020).

TGA was used to evaluate the approximate composition ratio of material and its thermal stability in oxygen-free environment. **Figure 3c** shows the results of TGA for materials GO, MGO, MP and PMGO. A significant weight loss was observed at temperature range of 153 - 202 ℃, which can be attributed to some labile substances such as bound water. Furthermore, it was noted that the higher proportions of Fe_3O_4 and HAP in PMGO materials resulted in less mass loss rate of material. When the temperature rose to 800 ℃, the weight loss of GO, MGO, MP, PMGO reached 75.24%, 39.82%, 1.81% and 18.06%, respectively. From these data, it could be speculated that the weight loss of PMGO were mainly attributed to the oxidation of GO (Szymczyk et al., 2019). Thus, it could be inferred that the relative content of GO in PMGO was approximately 20%.

Pore size, pore volume and specific surface area of materials MP, PMGO, PMGO-b, MP+GO were measured by BET-N_2 adsorption test (Table S3, **Figure 3d** and **Figure 3e**). Due to the load of GO, isotherm was changed from type II (MP) (Ahsan et al., 2020b) to type IV (PMGO) Li et al., 2011). Specific surface area increased from 84.21 to 158.72 m^2/g, while pore size decreased from 21.10 to 0.41 nm and pore volume decreased from 0.44 to 0.25 cm^3/g after ?????MP, PMGO or what? 谁和谁在比？ GO addition not only inhibited the self-polymerization of PMGO for an increased microporous structure, but also improved its space utilization rate,. All of these benefit the improvement of the adsorption capacity of PMGO (Ahsan et al., 2019). Compared with MP, the specific surface area of MP+GO had almost no change (84.11 m^2/g). However, both pore size and pore volume of PMGO were reduced with increased specific surface area, indicating the synthesis of PMGO is not to be a simple mixture of MP and GO. This increased specific surface area is conducive to adsorption capacity improvement (Cui et al., 2015).

Figure 3f shows the magnetism of PMGO-a (11.62 emu/g), PMGO-c (treatment under pH = 2.06, 10.47 emu/g) and PMGO-b5 (after 5 cycles of adsorption and recovery, 7.44 emu/g) byusing VSM., PMGO still maintained 90.10% magnetism under acidic conditions and 64.03%magnetism after five-cycle Pb^{2+} adsorption , implying that PMGO with an enormous application potential..

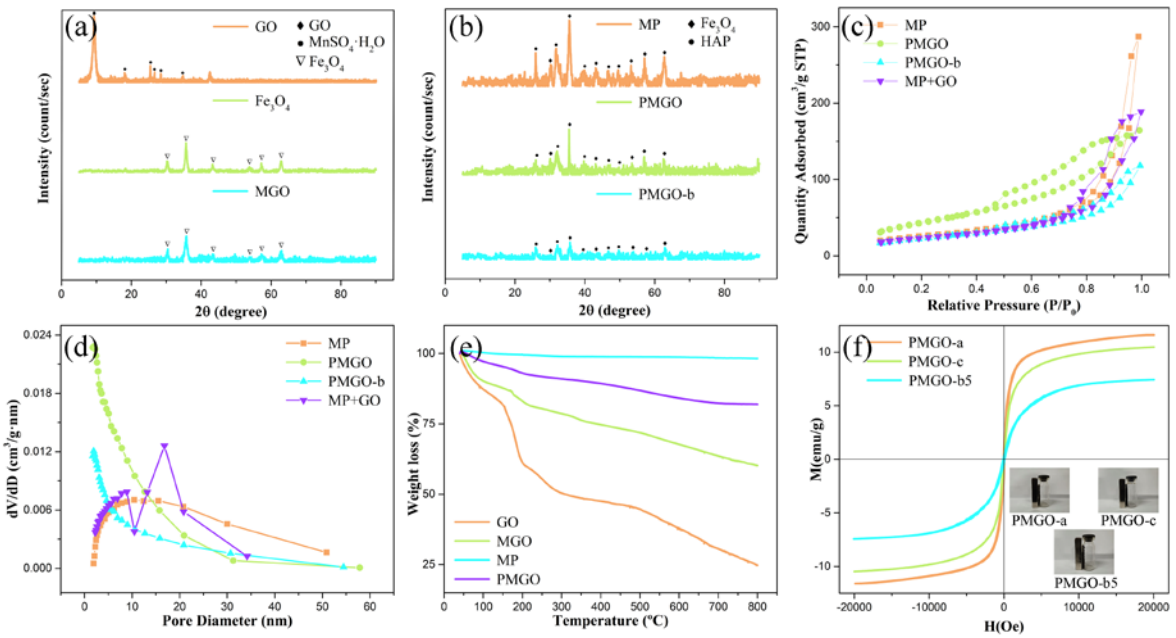

Figure 3. Material characterization (**a** and **b** show the XRD patterns of GO, M, MGO, MP, PMGO and PMGO-b; **c** and **d** show the BET results of MP, PMGO, PMGO-b and MP+GO; **d** shows the TGA result of GO, MGO, MP and PMGO; **f** shows the VSM spectrum of PMGO-a, PMGO-c and PMGO-b5).

3.2. Optimization of GO content in PMGO and Pb2+ adsorption conditions by PMGO

To provide reference for the subsequent experiments, the effect of GO content in PMGO on Pb2+ adsorption and adsorbent dosage on the adsorption capacity of PMGO were studied.

3.2.1. Effects of GO content in PMGO on Pb2+ adsorption

The optimal content of GO in PMGO was determined under the condition of 25 ℃, 180 rpm and 300 mg/L Pb^{2+} solution. The results in Figure S4a indicate that the adsorption capacity of PMGO reached maximum (e.g. 249.64 mg/g) when 0.2 g GO was added into ?? g of PM during synthesis. The $-COO^-$ functional groups of GO provide active sites for the adhesion of HAP. The monolayer structure of GO increased the attached quantity of HAP, thus improving the adsorption capacity of PMGO. When the GO dosage to MPwas higher than 0.2 g, the active

sites of GO for attachment of HAP were saturated. Thus the further increase in GO content could not increase the adsorption capacity of PMGO. PMGO with 0.2 g GO dosage was selected for subsequent experiments.

When the pH of Pb^{2+} solution is higher than 6.00 (Vergili et al., 2013), Pb^{2+} can combine with hydroxide to form $Pb(OH)_2$, resulting in the lowered Pb^{2+} concentration in the solution. But in this case, Pb2+ is reduced by precipitation instead of adsorption. To rule out the possibility of precipitation, pH of the Pb^{2+} solution before and after adsorption were measured. It is found that the pH before adsorption (pH = 4.82) and after adsorption (pH = 5.76) didn't reach the actual precipitation pH value. Therefore, it is reasonable to believe that Pb2+ removal is only caused by adsorption.

3.2.2. Adsorbent Dosage on Pb2+ adsorption

It is believed that Ca^{2+} in PMGO exchange with Pb^{2+} in solution. Thus, Pb^{2+} removal from the solution could be due to ion exchange. The more PMGO means more active sites for Pb^{2+} adsorption in the solution. Figure S4b shows the removal effect of Pb^{2+} under different dosage. It can be seen that with the increase in the PMGO dosage, Pb^{2+} removal efficiency of PMGO increased, but the adsorption capacity on Pb^{2+} decreased gradually. The relative exposure of the available active sites is decreased due to the increase of dosage (Asgarzadeh et al., 2015). 50 mg was thus chosen as the optimum dosage of PMGO for the subsequent

experiments.

To better compare the adsorption capacity of PMGO with some other magnetic materials, the adsorption capacities of different magnetic materials were listed in **Table 1**.

Table 1

Adsorption capacity of GO, PMGO and some other magnetic adsorbents on Pb^{2+} reported in literature .

Adsorbent	Adsorption Capacity, (mg/g)	Reference
Fe_3O_4-SiO_2-TiO_2	11.23	(Esfandiari et al., 2020)
PVP modified Fe_3O_4@SiO_2	18.84	(Wang et al., 2019a)
Magnetic Hydrochar	223.14	(Kazak and Tor, 2020)
GO	70.02 ± 5.55	Present study
M	79.98 ± 7.01	Present study
MGO	99.64 ± 12.97	Present study
MP	165.69 ± 5.93	Present study
PMGO	249.64 ± 1.49	Present study

The successful synthesis of PMGO is verified by comparing the adsorption capacity between GO (70.02 mg/g), MP (165.69 mg/g) and PMGO (249.64 mg/g). From BET analysis, it is known that the specific surface area of PMGO is about twice of that of MP, corresponding 1.5 times adsorption capacity. GO increases the adsorption capacity of PMGO primarily through increasing its active sites. Furthermore, compared with SiO_2 cladding, the GO load makes the material more functional.

3.3. Adsorption capacity and dissolution behavior of PMGO and MP at different pHs

Both HAP and Fe_3O_4 dissolve easily under acidic conditions, (Deratani et al., 2020; Sun

et al., 2016). However, when they bind with GO, dissolvability could be reduced due to strong bonds between GO, and HAP and Fe_3O_4. Thus, Pb^{2+} adsorption by PMGO under acidic conditions with pH from1 to 8 was investigated. In addition, ions such as Ca^{2+}, Fe^{3+}, K^+ and Mn^{2+} in the solution were measured as well to understand the dissolution behavior of PMGO.

3.3.1. Pb^{2+} adsorption by PMGO and MP at pH above 4

It is found that neither PMGO nor MP dissolves when pH $\geq$ 4. Thus, the adsorption capacity of PMGO and MP was studied with pH above 4 and results are shown in Figure 4a. It can be seen that with the increase of solution pH, the adsorption capacity of PMGO gradually enhanced. When pH is above 5.95, Pb^{2+} begins to hydrolyzes, which became more serious with the further increase in solution pH (Vergili et al., 2013). Concurrently, the concentration of Pb^{2+}, i.e. C_o in Equation (1), was reduced due to the hydrolysis of Pb^{2+}, limiting the adsorption by PMGO. Compared with PMGO, MP had lower Pb^{2+} adsorption capacity, which was only 178.40 mg/g. In addition, its Pb^{2+} adsorption capacity started to decline from pH of 6.97, higher than pH of 5.95 for PMGO. This indicates that the addition of GO enhanced Pb^{2+} adsorption.

To investigate the dissolution behavior of HAP and Fe_3O_4, the concentrations of Ca^{2+} and Fe^{3+} in the solution were measured in Pb^{2+} adsorption experiments by PMGO. The results in **Figure 4b** show that Ca^{2+} concentration increased slowly with the decrease in initial solution

pH, which might be attributed to the increased H^+ concentration with the pH decrease. Ca^{2+} concentration reached 42.41 mg/L in solution with PMGO and 33.51 mg/L withMP at initial pH of 3.97. In addition, as shown in **Figure 4c**, when pH was above3.97, no Fe^{3+} in solution was detected, suggesting Fe^{3+} in PMGO and MP did not dissolve , and.

3.3.2. Pb^{2+} adsorption by PMGO and MP at pH < 4

When the initial pH of solution was lower than 3.97, MP began to dissolve, and white, brown precipitates appeared in the solution at initial pH of3.07. At initial solution pH of 2.06, MP was difficult to be separated from solution by an external magnetic field, indicating the loss of magnetism of Fe_3O_4 probably due to dissolution of Fe_3O_4. In contrast, no precipitates were observed in the solution with PMGO as adsorbents. Meanwhile, PMGO still maintained integrity and easy separation property by external magnetic field. As shown in **Figure 4d**, the reduction in Pb^{2+} concentration in solution with MP as adsorbents reached the maximum, i.e. 297.96 mg/L, at the initial pH of 3.07 while the reduction of Pb^{2+} concentration with PMGO as adsorbents was only 143.04 mg/L and it decreased with the increase in the solution initial pH..

Figure 4e and **Figure 4f** show the dissolution behavior of Ca^{2+} and Fe^{3+} in PMGO andMP under acidic conditions. At initial solution pH of 3.97, the concentration of Ca^{2+} in the solution with PMGO as adsorbents was much higher than that with MP because of the stronger ion

exchange between H+ in the solution and Ca^{2+} in adsorbents. ,. While at initial pH lower than 3.97, HAP dissolved gradually, and Ca^{2+} concentration in the solution with MP as adsorbents was basically same as that with PMGO. As shown in **Figure 4f**, at initial solution pH of 1.01, the concentration of Fe^{3+} in the solution with MP as adsorbents is 58.29 mg/L, which is significantly higher than 24.34 mg/L in the solution with PMGO as adsorbents, indicating that Fe in MP dissolved more than in PMGO

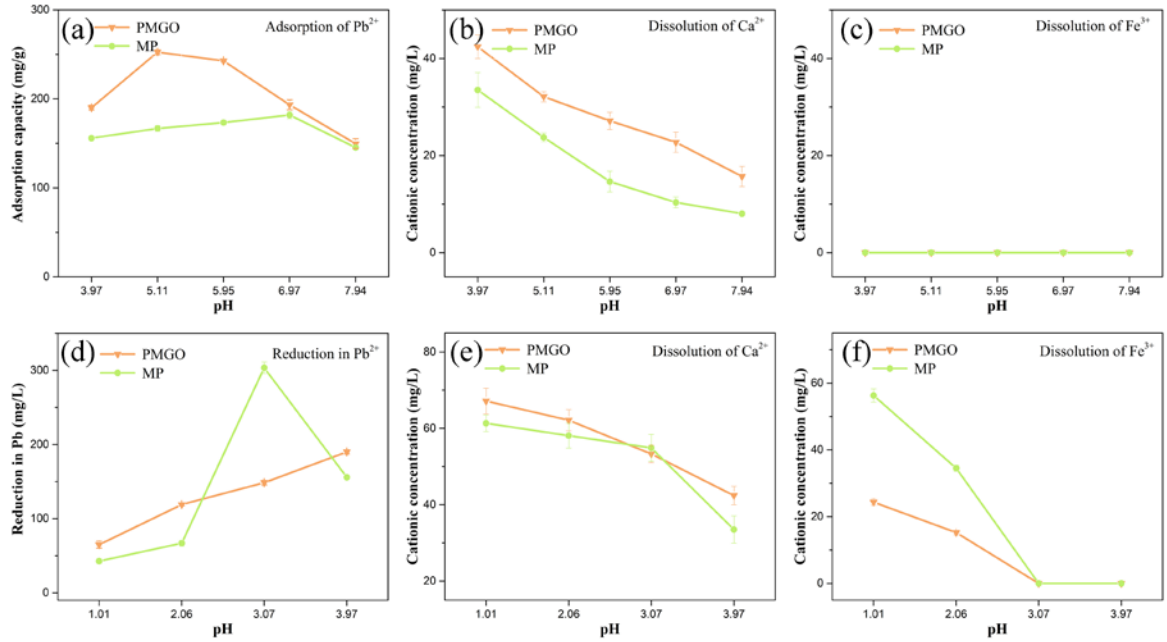

Figure 4. Effect of pH on adsorption capacity and dissolution behavior (**a** shows the adsorption capacity of adsorbents at pH of 4 - 8, **b** shows the concentration of Ca^{2+} dissolved at pH of 4 - 8, **c** shows the concentration of Fe^{3+} dissolved at pH of 4 - 8, **d** shows the adsorption capacity of adsorbents at pH of 1 - 4, **e** shows the concentration of Ca^{2+} dissolved at pH of 1 - 4, **f** shows the concentration of Fe^{3+} dissolved at pH of 1 - 4).

It was also found that solution pH after Pb2+ adsorption increased for example from 3.07 to 3.61 with PMGO as adsorbents while from 3.07 to 4.73 with MP as adsorbents.

3.3.3. Dissolution behavior of PMGO and MP

As shows in Equation (4), with the increase in H^+ concentration in the solution, HAP dissolves with Ca^{2+}, and PO_4^{3-} in HAP transferred into the solution. This explains why Ca^{2+} concentration increased at lower pH and why precipitates of $Pb_3(PO_4)_2$ (as shown in Equation (5)) formed to reduce Pb^{2+} concentration dramatically.

$$Ca_{10}(PO_4)_6(OH)_2 + 2H^+ \leftrightarrow 10Ca^{2+} + 6{PO_4}^{3-} + 2H_2O \quad (4)$$

$$2{PO_4}^{3-} + 3Pb^{2+} \leftrightarrow Pb_3(PO_4)_2 \quad (5)$$

At initial solution pH lower than 3.07, with the further increase in H^+ concentration, the lattice of Fe_3O_4 is also being destroyed as HAP, resulting in and a large amount of Fe^{3+} released from absorbent to the solution as shows in Equation (6). Fe^{3+} concentration in the solution therefore increased with the decrease in pH. Moreover, Fe^{3+} is more likely to react with PO_4^{3-} than Pb^{2+} as shown in Equation (7). With the increase in Fe^{3+} concentration in the solution, the binding of Pb^{2+} with PO_4^{3-} as shown in Equation (5) was inhibited and and Fe^{3+} reacted with PO_4^{3-} to form $FePO_4$. This explains why brown precipitates appeared at initial solution pH of 3.07 with sudden decrease of Pb2+ concentration when MP was used as adsorbents.

$$Fe_3O_4 + 8H^+ \leftrightarrow 2Fe^{3+} + Fe^{2+} + 4H_2O \quad (6)$$

$$2Fe^{3+} + Pb_3(PO_4)_2 \leftrightarrow 2FePO_4 + 3Pb^{2+} \quad (7)$$

In contrast, the adsorption capacity of Pb^{2+} by PMGO didn't fluctuate as drastically as by MP . Ca^{2+} concentration due to the increase in H^+ only showed a slowly rising trend, and Fe^{3+}

concentration in PMGO processing solution was also lower than that of MP. No white and brown precipitates were observed at under acidic conditions because large amounts of -COO^- on GO surface provide buffer role to impede the dissolution of PMGO, i.e. the -OH and -COOH on GO inhibits the flow of Ca, Fe from absorbents to the solution.

3.4. Kinetic, Isothermal and Thermodynamic models for Pb2+ adsorption by PMGO and MP

kinetic, isothermal and thermodynamic models are usually used to understand the physicochemical properties of adsorbents and associated adsorption mechanism (Ahsan et al., 2019). In this part, by comparing the model parameters of PMGO and MP, the adsorption mechanism of PMGO was explained and its superior performance was proved.

3.4.1. Kinetic Study on Pb^{2+} adsorption by PMGO and MP

To investigate the effects of adsorption time on adsorption capacity, the concentration of Pb^{2+} in solution with different adsorption durations was measured. Pseudo first-order kinetic, pseudo second-order kinetic and intra-particle diffusion models were used to fit experimental adsorption data. Experimental and fitting results are shown in Figure S6, and the adsorption kinetic parameters are summarized in **Table 2** and Table S4. It is found that the pseudo second-order kinetic model (R^2 = 0.9972) can better reflect the adsorption than the pseudo first-order kinetic model (R^2 = 0.9723) with the theoretical adsorption capacity ($q_{e,cal}$, 274.73 mg/g) more

close to the experimental value ($q_{e,exp}$, 270.02 mg/g). This suggests that the adsorption is mainly through chemical adsorption (Fan et al., 2019). Interestingly, GO addition does not only increase the adsorption capacity (PMGO, 270.02 mg/g; MP, 173.51 mg/g), but also speed up the adsorption rate. This is because that GO has active adsorption sites for Pb2+ adsorption as well and thus the addition of GO can increases the total adsorption active sites of PMGO. With the intra-particle diffusion model, it is observed that the slope decreased and the intercept increased, suggesting the increased ion diffusion resistance of adsorbents after Pb2+ adsorbing. Since the curve displayed with experiment results didn't pass through the origin of coordinates, it could be speculated that diffusion isn't the only speed limiting factor for adsorption (Ahsan et al., 2019).

Table 2

Adsorption kinetic parameters of Pb^{2+} by PMGO and MP.

Kinetic model	Pseudo first-order			Pseudo second-order		
Parameters	Q_{e1} ($mg \cdot g^{-1}$)	k_1 (min^{-1})	R^2	Q_{e2} ($mg \cdot g^{-1}$)	k_2 ($g \cdot mg^{-1} \cdot min^{-1}$)	R^2
PMGO	254.88	0.0758	0.9723	274.73	1.8×10^{-4}	0.9972
MP	165.11	0.0649	0.9689	178.40	2.3×10^{-4}	0.9961

3.4.2. Isotherm Study on Pb^{2+} adsorption by PMGO and MP

Isotherm model is usually used to describe the distribution of adsorbates between solid and liquid phases in equilibrium. The adsorption capacities of PMGO and MP, with 200 - 800 mg/L Pb^{2+} concentrations at 288.15 K, 298.15 K and 308.15 K, respectively, were investigated

(Figure S7). Langmuir and Freundlich models were used to fit experimental results, and model parameters are summarized in **Table 3**. Langmuir model (R^2 = 0.9996) gives a better fit than the Freundlich model (R^2 = 0.9424), indicating that the surface of the adsorbents is energetically homogeneous and independent each other (Thanh et al., 2018). With the Langmuir model, q_m increased gradually with the rise in the reaction temperature, thus, it is inferred that the adsorption of PMGO is an endothermic reaction. Moreover, *1/n* in the Freundlich model is often used to represent the bond distribution. The smaller *1/n* is, the more favorable of reaction is (Ahsan et al., 2019). In this study, *1/n* of both PMGO and MP were less than 1, so both reactions were favorable under the current conditions. K_F is often to express the strength between adsorbents and adsorbates. The higher value of K_F represents the stronger capacity of the adsorbents (Fan et al., 2019). In this study, K_F value of PMGO (194.55 mg/g) is higher than MP (123.36 mg/g), indicating a stronger adsorption capacity. This is consistent with the adsorption experiments.

Table 3

Adsorption isotherm parameters of Pb^{2+} by PMGO and MP.

Adsorbent	T(K)	Langmuir constants			Freundlich constants		
		q_m ($mg \cdot g^{-1}$)	k_L ($L \cdot mg^{-1}$)	R^2	k_F ($mg \cdot g^{-1}$)	1/n	R^2
PMGO	288.15	277.78	0.1237	0.9994	182.9842	0.0669	0.9962
	298.15	284.12	0.1726	0.9996	194.5521	0.0674	0.9424
	308.15	303.03	0.1650	0.9994	201.4417	0.0642	0.8953
MP	288.15	185.19	0.0548	0.9994	116.7576	0.0683	0.9571
	298.15	192.31	0.0584	0.9993	123.3591	0.0639	0.9369

308.15	196.08	0.0612	0.9994	127.7021	0.0650	0.9631

3.4.3. Thermodynamic Study on Pb^{2+} adsorption by PMGO and MP

To further understand the adsorption reaction mechanism, standard enthalpy change (*ΔH*), standard entropy change (*ΔS*) and Gibbs free energy change (*ΔG*) are obtained from the Van't hoff equation (Masson et al., 2017) and values are summarized in **Table 4**. It can be seen that *ΔS* is above 0 and *ΔS* of PMGO is larger than that of MP, indicating the increased randomness at the adsorbent-adsorbate interface of PMGO for Pb^{2+} adsorption (Ahsan et al., 2019). *ΔH* of adsorbents is above 0 as shown in Table 4 , suggesting that the adsorption is endothermic (Khatoon et al., 2018) while *ΔG* is less than 0, indicating spontaneous adsorption . From the thermodynamic parameters, it can be concluded that the Pb2+ adsorption by PMGO and MP are thermodynamically favorable, and the increase in temperature is beneficial to the adsorption (Ahsan et al., 2019).

Table 4

Adsorption thermodynamic parameters of Pb^{2+} by PMGO and MP.

PMGO				MP			
T(K)	ΔG (kJ mol^{-1})	ΔH (kJ mol^{-1})	ΔS (J $mol^{-1}K^{-1}$)	T(K)	ΔG (kJ mol^{-1})	ΔH (kJ mol^{-1})	ΔS (J $mol^{-1}K^{-1}$)
288.15	-3.53			288.15	-0.39		
298.15	-4.02	10.58	48.98	298.15	-0.51	3.79	14.44
308.15	-4.51			308.15	-0.66		

3.5. Interference of other metal ions on Pb2+ adsorption by PMGO and recyclability of PMGO

In the practical application of adsorbents, other cations in wastewater might interfere Pb2+ adsorption due to the competition for the adsorption active sites. In addition, the high recyclability of magnetic adsorbents can reduce the absorbent cost. Thus. This part addressed these two points.

3.5.1. **Interference of other metal ions on Pb2+ adsorption by PMGO**

As shown in Figure S8, it can be found that: (I)Monovalent ions (Na^+, K^+) have little influence on the Pb2+ adsorption capacity of PMGO; (II)Divalent ions (Ca^{2+}, Mg^{2+}) have a higher influence than monovalent ions on the adsorption capacity, and the effect of Ca^{2+} is much greater than that of Mg^{2+}; (III)Trivalent ion (Fe^{3+}) has the most influence among all metal ions. In general, the influence of cations on Pb^{2+} adsorption by PMGO can be ranked as: $Fe^{3+} > Ca^{2+} > Mg^{2+} > K^+ > Na^+$, i.e. trivalent ion > divalent ion > monovalent ion. Moreover, similar phenomenon was also observed in MP anti-interference experiment, but MP's anti-interference ability is weaker than that of PMGO. The addition of GO increased the exposed quantity of Ca in PMGO, and enhanced ion exchange with H+ in the solution, which thus increased the anti-interference ability of PMGO.

3.5.2. Recyclability of PMGO for Pb2+ adsorption

As shown in Figure S9a, magnetic separation process is widely used in wastewater treatment because magnetic adsorbents can be separated with an magnetic field for recycling

441 and thus it can reduce the cost of adsorbents.

442 Different alkaline eluents were tested for the recycling of PMGO and the results of
443 recyclability are summarized in Table S5. It can be found that NaOH and $Ca(OH)_2$ eluting led
444 to ideal recovery performance (94.31 and 137.38 mg/g by PMGO, respectively, while 49.24
445 and 76.49 mg/g by MP respectively).

446 Thus, $Ca(OH)_2$ was selected as the elute to regenerate PMGO for five times Each time,
447 PMGO was recovered by an external magnet after adsorption. From Figure S9b and Figure S9c,
448 it can be seen that PMGO after 5 cycles still maintained 97.49 mg/g adsorption capacity, ??%
449 of the original adsorption capacity, while MP only maintained 45.61 mg/g adsorption capacity.
450 After each adsorption, it was noticed that the mass of adsorbents increased because heavy ion
451 Pb^{2+} in the solution replaced Ca^{2+} in the adsorbents. In addition the quality of adsorbents
452 decreased after each desorption under alkaline conditions Pb between $-COO^-$ and HAP was
453 replaced by Ca^{2+}. Similar studies (Ain et al., 2020; Cui et al., 2015) reported that Fe_3O_4 and
454 HAP had low desorption efficiency in the solution, thus, it reduced the migration of pollutants
455 in wastewater to where? . Briefly, PMGO can be used as an effective adsorbent for Pb2+
456 removal from acid wastewater and can be reasonably recycled for a certain times.

457 **3.6. The exploration of Pb2+ adsorption mechanism by PMGO and MP**

458 The adsorption mechanisms of heavy metal are complicated, which can be generally

459 classified into four types (Thanh et al., 2018), i.e. ion exchange, surface complexation,
460 electrostatic interaction, dissolution/precipitation. In addition, the competition mechanism of
461 other cations with Pb^{2+} adsorption is also different. To authors' knowledge, the study on the
462 adsorption mechanism of Pb2+ is little. To develop the practical application of PMGO, it is
463 crucial to understand these mechanisms. In this part, these mechanisms were discussed.

464 3.6.1. Ion Exchange mechanism involved in PMGO and MP

465 Pb^{2+} adsorption by HAP can be explained by ion exchange between Ca2+ and Pb2+ with
466 equal moles. The surfaces of HAP provide nucleation sites for new crystalline phases as
467 shown below (Wang et al., 2019b):

468 $$Ca_{10}(PO_4)_6(OH)_2 + xPb^{2+} \leftrightarrow Ca_{10-x}Pb_x(PO_4)_6(OH)_2 + xCa^{2+} \quad (8)$$

469 To verify this mechanism in Pb2+ adsorption by PMGO, some additional experiments
470 (PMGO-CK, MP-CK) were carried out. Under the same experimental conditions, PMGO and
471 MP were added to 50 mL DI water and the Ca^{2+} concentration in the water was measured after
472 3 h oscillation.

473 It is found that the concentration of Ca^{2+} in DI water was significantly lower than that in
474 the Pb2+ adsorption experiment solution (PMGO, PMGO-CK, MP, MP-CK were 32.65, 2.57,
475 22.36, 2.57 mg/L, respectively). It can thus be inferred that ion exchange between Ca2+ and
476 Pb2+ took place, which is one of the Pb2+ adsorption mechanisms by PMGO. From the

exchanged Ca2+ concentration, it can be calculated that ion exchange mechanism accounts for about 62.15% (PMGO) and 62.72% (MP) of the total Pb2+ adsorption.

3.6.2. Surface Complexation mechanism involved in PMGO and MP

Uheida et al (Uheida et al., 2006) reported that the surface complexation can take place between the positive ions in the solution and the protons of hydroxyl groups on adsorbent surface. In the PMGO adsorption experiment, the surfaces of Fe_3O_4, HAP and GO could provide protons for the complexation with Pb^{2+}. This mechanism was reported as the initial rapid step of the adsorption of Pb^{2+}. (Fernane et al., 2010)while the subsequent slower adsorption is related to Ca2+/Pb2+ exchange between HAP in PMGO and water solution.

3.6.3. Electrostatic Interaction mechanism involved in PMGO and MP

HAP and Fe_3O_4 show a certain buffering capability in solution, which can be mainly expressed by the following equations (Bagbi et al., 2016; Smiciklas et al., 2006):

$$\equiv \mathrm{PO^-} + \mathrm{H^+} \leftrightarrow \mathrm{POH} \quad (9)$$

$$\equiv \mathrm{CaOH_2^+} \leftrightarrow \mathrm{CaOH} + \mathrm{H^+} \quad (10)$$

$$\equiv \mathrm{FeOH} + \mathrm{H^+} \leftrightarrow \mathrm{FeOH_2^+} \quad (11)$$

$$\equiv \mathrm{FeOH} \leftrightarrow \mathrm{FeO^-} + \mathrm{H^+} \quad (12)$$

Pb^{2+}, $Pb(OH)^+$ and $Pb(OH)_2$ are the major forms of Pb at pH of 1 - 7. At pH lower than 5, Pb exists mainly in the form of Pb^{2+}, thus, it could be removed from solution mainly via ion

exchange. At pH above 5, Pb^{2+} is converted into $Pb(OH)^{+}$ and prone to precipitate as $Pb(OH)_2$. Thus, Pb2+ could be removed by precipitation due to high pH. At this time, the adsorbent still has a favorable adsorption capacity for Pb^{2+}.

Furthermore, at pH lower than 5, PMGO is positively charged as $CaOH_2^{+}$, $FeOH_2^{+}$, which could repulse with Pb2+ by electrostatic repulsion and thus reduce the Pb2+ adsorption and neutral ≡ POH^0 are predominated on the surface sites of PMGO, and electrostatic repulsion under this condition inhibits the adsorption of Pb^{2+}. At pH above 5, the positive charges on the adsorbent surface decrease,and the adsorbent becomes relatively neutral. With the pH increase above 7, PMGO is covered by negative charge, and the electrostatic attraction between Pb2+ and negative charges is able to increase Pb2+ adsorption. In the anti-interference experiment, PMGO maintained excellent adsorption capacity of Pb^{2+}, so the electrostatic mechanism might not be involved for Pb2+ adsorption.

3.6.4. Dissolution/Precipitation mechanism involved in PMGO and MP

It was reported that HAP can dissolve in solution by ionization, and then react with Pb^{2+} to form precipitates (Dong et al., 2010). Dong et al (Dong et al., 2020).found that the XRD peaks of HAP after Pb2+ adsorption decreased, while the peaks corresponding to phosphate appeared, confirming the existence of dissolution/precipitation mechanism. In our research, although the XRD peaks of PMGO decreased after Pb2+ adsorption, no obvious phosphate

peak was observed. Therefore, this mechanism could not be important in Pb2+ adsorption process by PMGO.

3.6.5. Anti-interference Mechanism involved in PMGO and MP

To further understand the interference mechanism of other metal ions on Pb2+ adsorption by PMGO, the change of other cations concentrations in anti-interference experiments were calculated and listed in Table S6.

From the data in Table S6, phenomenon in anti-interference experiments can be explained by electrostatic repulsion (Li et al., 2020) (Na^+, K^+, Mg^{2+}), common ion effect (Wu et al., 2019) (Ca^{2+}) and competitive adsorption (Nishida et al., 2017) (Fe^{3+}). In our study, the MPGO mainly adsorbs Pb^{2+} through chemical action, so electrostatic repulsion has little effect on its adsorption capacity. Conversely, common ion effect and competitive adsorption might have a significant interference on Pb^{2+} adsorption. The increase in Ca^{2+} concentration inhibited ion exchange, reducing the adsorption capacity of MPGO. From the solubility product constant of $FePO_4$ and $Pb_3(PO_4)_2$, it can be known that the ion exchange between Fe^{3+} and Ca^{2+} is much easier than that between Pb^{2+} and Ca^{2+}. Thus Fe^{3+} has the maximal negative influence on the adsorption of Pb^{2+} by MPGO.

For metal ions such as Na^+, K^+, and Mg^{2+}, PMGO still possessed 211.87 (Na^+), 208.68

(K^+) and 201.13 mg/g (Mg^{2+}) adsorption capacity when their concentration was increased to 0.1 M,. When the initial concentrations of other cations were 0.01 M, the concentration of these ions in water solution ? decreased after Pb2+ adsorption, indicating that adsorption is inhibited by electrostatic repulsion, the Pb2+ adsorption capacity of PMGO was reduced. It can be understood that when these cations concentrations increased, more Ca^{2+} in MPGO ? released into solutions due to ion exchange, resulting in higher Ca^{2+} in the solution than that of the solution without interfering metal ions. This phenomenon can be attributed to the salt effect (Sadeghi et al., 2016), by which the increase of total ion concentration in solution can improve the dissociation of weak electrolyte molecules.

4. Conclusion

A novel nanoscale magnetic absorbent, i.e. MPGO, was synthesized for Pb2+ adsorption from acid wastewater at low pH. GO integration into MP effectively inhibited the dissolution of Fe_3O_4 under acidic conditions, which thus ensures the maintenance of magnetism of absorbent for separation and recycling. This has important implication for practical application of magnetic absorbent to acid wastewater. As one of the most promising materials, GO enhances the adsorption capacity of magnetic materials by inhibiting its self-polymerization. Meanwhile, due to the buffer roles played by GO, magnetic material demonstrated strong acid resistance. This work developed a novel approach to expand the application domain of magnetic absorbent

by integrating GO for metal ion removal from acid wastewater.

Acknowledgements

The study was supported by Sichuan Science and Technology Program (2019YJ0514) and scientific research starting project of SWPU (2018QHZ018). The authors would like to thank Shiyanjia Lab (www.shiyanjia.com) and Analytical & Testing Center, Sichuan University, P. R. China. The authors would also like to thank the editor for handling this article and anonymous reviewers for their constructive comments for paper improvement.

References

Ahsan MA, Jabbari V, Imam MA, Castro E, Kim H, Curry ML, et al. Nanoscale nickel metal organic framework decorated over graphene oxide and carbon nanotubes for water remediation. Sci Total Environ 2020a; 698: 134214.

Ahsan MA, Jabbari V, Islam MT, Turley RS, Dominguez N, Kim H, et al. Sustainable synthesis and remarkable adsorption capacity of MOF/graphene oxide and MOF/CNT based hybrid nanocomposites for the removal of Bisphenol A from water. Sci Total Environ 2019; 673: 306-317.

Ahsan MA, Puente Santiago AR, Hong Y, Zhang N, Cano M, Rodriguez-Castellon E, et al. Tuning of Trifunctional NiCu Bimetallic Nanoparticles Confined in a Porous Carbon Network with Surface Composition and Local Structural Distortions for the Electrocatalytic Oxygen Reduction, Oxygen and Hydrogen Evolution Reactions. Journal of the American Chemical Society 2020b; 142: 14688-14701.

Ahsan MA, Puente Santiago AR, Sanad MF, Mark Weller J, Fernandez-Delgado O, Barrera LA, et al. Tissue paper-derived porous carbon encapsulated transition metal nanoparticles as advanced non-precious catalysts: Carbon-shell influence on the electrocatalytic behaviour. J Colloid Interface Sci 2021; 581: 905-918.

Ain QU, Zhang H, Yaseen M, Rasheed U, Liu K, Subhan S, et al. Facile fabrication of hydroxyapatite-magnetite-bentonite composite for efficient

adsorption of Pb(II), Cd(II), and crystal violet from aqueous solution. Journal of Cleaner Production 2020; 247: 119088.

Akın Sahbaz D, Yakar A, Gündüz U. Magnetic Fe3O4-chitosan micro- and nanoparticles for wastewater treatment. Particulate Science and Technology 2018; 37: 732-740.

Asgarzadeh S, Rostamian R, Faez E, Maleki A, Daraei H. Biosorption of Pb(II), Cu(II), and Ni(II) ions onto novel lowcostP. eldaricaleaves-based biosorbent: isotherm, kinetics, and operational parameters investigation. Desalination and Water Treatment 2015; 57: 14544-14551.

Bagbi Y, Sarswat A, Mohan D, Pandey A, Solanki PR. Lead (Pb2+) adsorption by monodispersed magnetite nanoparticles: Surface analysis and effects of solution chemistry. Journal of Environmental Chemical Engineering 2016; 4: 4237-4247.

Beygmohammdi F, Nourizadeh Kazerouni H, Jafarzadeh Y, Hazrati H, Yegani R. Preparation and characterization of PVDF/PVP-GO membranes to be used in MBR system. Chemical Engineering Research and Design 2020; 154: 232-240.

Cui L, Wang Y, Gao L, Hu L, Yan L, Wei Q, et al. EDTA functionalized magnetic graphene oxide for removal of Pb(II), Hg(II) and Cu(II) in water treatment: Adsorption mechanism and separation property. Chemical Engineering Journal 2015; 281: 1-10.

Deratani A, Taleb S, Ikhou D, Taleb Z, Adjdir M, Kadeche A, et al. Lead and cadmium removal by adsorption process using hydroxyapatite porous materials. Water Practice and Technology 2020; 15: 130-141.

Dong L, Zhu S, Xia M, Chu Y, Wang F, Lei W. Molecular dynamics simulations of the binging affinity of 1-hydroxyethane-1, 1-diphosphonic acid (HEDP) with nano-hydroxyapatite and the uptake of Cu(2+) by HEDP-HAP hybrid systems. J Hazard Mater 2020; 383: 121206.

Dong L, Zhu Z, Qiu Y, Zhao J. Removal of lead from aqueous solution by hydroxyapatite/magnetite composite adsorbent. Chemical Engineering Journal 2010; 165: 827-834.

Esfandiari N, Kashefi M, Mirjalili M, Afsharnezhad S. Role of silica mid-layer in thermal and chemical stability of hierarchical Fe3O4-SiO2-TiO2 nanoparticles for improvement of lead adsorption: Kinetics, thermodynamic and deep XPS investigation. Materials Science and Engineering: B 2020; 262: 114690.

Fan S, Huang Z, Zhang Y, Hu H, Liang X, Gong S, et al. Magnetic chitosan-hydroxyapatite composite microspheres: Preparation, characterization, and application for the adsorption of phenolic substances. Bioresour Technol 2019; 274: 48-55.

Fang X, Wang S, Li Y, Liu X, Li X, Lin S, et al. NH2-functionalized carbon-coated Fe3O4 core–shell nanoparticles for in situ preparation of robust polyimide composite films with high dielectric constant, low dielectric loss, and high breakdown strength. RSC Advances 2016; 6: 107533-107541.

Fernane F, Mecherri MO, Sharrock P, Fiallo M, Sipos R. Hydroxyapatite interactions with copper complexes. Materials Science and Engineering: C 2010; 30: 1060-1064.

Ferrari AC. Raman spectroscopy of graphene and graphite: Disorder, electron–phonon coupling, doping and nonadiabatic effects. Solid State Communications 2007; 143: 47-57.

Guo Y, Deng J, Zhu J, Zhou X, Bai R. Removal of mercury(ii) and methylene blue from a wastewater environment with magnetic graphene oxide: adsorption kinetics, isotherms and mechanism. RSC Advances 2016; 6: 82523-82536.

Gupta R, Sood AK, Metcalf P, Honig JM. Raman study of stoichiometric and Zn-dopedFe3O4. Physical Review B 2002; 65.

Hou Y, Lv S, Liu L, Liu X. High-quality preparation of graphene oxide via the Hummers' method: Understanding the roles of the intercalator, oxidant, and graphite particle size. Ceramics International 2020; 46: 2392-2402.

Islam MT, Saenz-Arana R, Hernandez C, Guinto T, Ahsan MA, Kim H, et al. Adsorption of methylene blue and tetracycline onto biomass-based material prepared by sulfuric acid reflux. RSC Advances 2018; 8: 32545-32557.

Kazak O, Tor A. In situ preparation of magnetic hydrochar by co-hydrothermal treatment of waste vinasse with red mud and its adsorption property for Pb(II) in aqueous solution. Journal of Hazardous Materials 2020; 393: 122391.

Khatoon A, Uddin MK, Rao RAK. Adsorptive remediation of Pb(II) from aqueous media using Schleichera oleosa bark. Environmental Technology & Innovation 2018; 11: 1-14.

Li Y, Zhang X, Zhang P, Liu X, Han L. Facile fabrication of magnetic bio-derived chars by co-mixing with Fe3O4 nanoparticles for effective Pb2+ adsorption: Properties and mechanism. Journal of Cleaner Production 2020; 262: 121350.

649 Li Z, Song D, Zhi J, Hu A. Synthesis of Ultrathin Ordered Porous Carbon through
650 Bergman Cyclization of Enediyne Self-Assembled Monolayers on Silica
651 Nanoparticles. The Journal of Physical Chemistry C 2011; 115: 15829-
652 15833.
653 López EO, Rossi AL, Bernardo PL, Freitas RO, Mello A, Rossi AM. Multiscale
654 connections between morphology and chemistry in crystalline, zinc-
655 substituted hydroxyapatite nanofilms designed for biomedical applications.
656 Ceramics International 2019; 45: 793-804.
657 Lovón-Quintana JJ, Rodriguez-Guerrero JK, Valença PG. Carbonate
658 hydroxyapatite as a catalyst for ethanol conversion to hydrocarbon fuels.
659 Applied Catalysis A: General 2017; 542: 136-145.
660 Lu HB, Campbell CT, Graham DJ, Ratner BD. Surface characterization of
661 hydroxyapatite and related calcium phosphates by XPS and TOF-SIMS.
662 Anal Chem 2000; 72: 2886-94.
663 Luo L, Yang Y, Li H, Ding R, Wang Q, Yang Z. Size characterization of silver
664 nanoparticles after separation from silver ions in environmental water using
665 magnetic reduced graphene oxide. Science of The Total Environment 2018;
666 612: 1215-1222.
667 Masson S, Vaulot C, Reinert L, Guittonneau S, Gadiou R, Duclaux L.
668 Thermodynamic study of seven micropollutants adsorption onto an
669 activated carbon cloth: Van't Hoff method, calorimetry, and COSMO-RS
670 simulations. Environ Sci Pollut Res Int 2017; 24: 10005-10017.
671 Nishida H, Kimata M, Ogata T, Kawai T. Malodors adsorption behavior of metal
672 cation incorporated hydroxyapatite. Journal of Environmental Chemical
673 Engineering 2017; 5: 2815-2819.
674 Panella B, Vargas A, Baiker A. Magnetically separable Pt catalyst for asymmetric
675 hydrogenation. Journal of Catalysis 2009; 261: 88-93.
676 Pudukudy M, Jia Q, Dong Y, Yue Z, Shan S. Magnetically separable and reusable
677 rGO/Fe3O4 nanocomposites for the selective liquid phase oxidation of
678 cyclohexene to 1,2-cyclohexane diol. RSC Advances 2019; 9: 32517-
679 32534.
680 Sadeghi R, Solaimani S, Ebrahimi N. Thermodynamic properties of anionic
681 surfactant/polymer/water systems with respect to polymer-surfactant
682 interactions and salting-effect of surfactant on polymer in aqueous
683 solutions. Fluid Phase Equilibria 2016; 425: 411-420.
684 Sanad MF, Shalan AE, Bazid SM, Abu Serea ES, Hashem EM, Nabih S, et al. A

graphene gold nanocomposite-based 5-FU drug and the enhancement of the MCF-7 cell line treatment. RSC Advances 2019; 9: 31021-31029.
Smiciklas I, Dimovic I, Mitric M. Removal of Co2+ from aqueous solutions by hydroxyapatite. Water Res 2006; 40: 2267-74.
Sun X, Yang L, Dong T, Liu Z, Liu H. Removal of Cr(VI) from aqueous solution using amino-modified Fe3O4-SiO2-chitosan magnetic microspheres with high acid resistance and adsorption capacity. Journal of Applied Polymer Science 2016; 133: n/a-n/a.
Szymczyk A, Paszkiewicz S, Typek J, Špitalský Z, Janowska I, Żołnierkiewicz G, et al. Magnetic Properties of Poly(trimethylene terephthalate ‐
block
‐ Poly(tetramethylene oxide) Copolymer Nanocomposites Reinforced by Graphene Oxide–Fe
3
O
4
Hybrid Nanoparticles. physica status solidi (a) 2019; 216: 1900402.
Talla D, Wildner M. Investigation of the kieserite–szomolnokite solid-solution series, (Mg,Fe)SO4·H2O, with relevance to Mars: Crystal chemistry, FTIR, and Raman spectroscopy under ambient and martian temperature conditions. American Mineralogist 2019; 104: 1732-1749.
Thanh DN, Novák P, Vejpravova J, Vu HN, Lederer J, Munshi T. Removal of copper and nickel from water using nanocomposite of magnetic hydroxyapatite nanorods. Journal of Magnetism and Magnetic Materials 2018; 456: 451-460.
Uheida A, Salazar-Alvarez G, Bjorkman E, Yu Z, Muhammed M. Fe3O4 and gamma-Fe2O3 nanoparticles for the adsorption of Co2+ from aqueous solution. J Colloid Interface Sci 2006; 298: 501-7.
Ulian G, Valdre G. Effect of mechanical stress on the Raman and infrared bands of hydroxylapatite: A quantum mechanical first principle investigation. J Mech Behav Biomed Mater 2018; 77: 683-692.
Vélez-Pérez LS, Ramirez-Nava J, Hernández-Flores G, Talavera-Mendoza O, Escamilla-Alvarado C, Poggi-Varaldo HM, et al. Industrial acid mine drainage and municipal wastewater co-treatment by dual-chamber microbial fuel cells. International Journal of Hydrogen Energy 2020; 45: 13757-13766.

Vergili I, Soltobaeva G, Kaya Y, Gönder ZB, Çavuş S, Gürdağ G. Study of the Removal of Pb(II) Using a Weak Acidic Cation Resin: Kinetics, Thermodynamics, Equilibrium, and Breakthrough Curves. Industrial & Engineering Chemistry Research 2013; 52: 9227-9238.

Wang L, Shen C, Cao Y. PVP modified Fe3O4@SiO2 nanoparticles as a new adsorbent for hydrophobic substances. Journal of Physics and Chemistry of Solids 2019a; 133: 28-34.

Wang Y, Li R, Liu W, Cheng L, Jiang Q, Zhang Y. Exploratory of immobilization remediation of hydroxyapatite (HAP) on lead-contaminated soils. Environ Sci Pollut Res Int 2019b; 26: 26674-26684.

Wen T, Wu X, Liu M, Xing Z, Wang X, Xu AW. Efficient capture of strontium from aqueous solutions using graphene oxide-hydroxyapatite nanocomposites. Dalton Trans 2014; 43: 7464-72.

Wu Z, Hou Y, Wu W, Ren S, Zhang K. Efficient Removal of Sulfuric Acid from Sodium Lactate Aqueous Solution Based on the Common-Ion Effect for the Absorption of SO2 of Flue Gas. Energy & Fuels 2019; 33: 4395-4400.

Xiong J, Di J, Li H. Charge steering in ultrathin 2D nanomaterials for photocatalysis. Journal of Materials Chemistry A 2020; 8: 12928-12950.

Xu D, Xiong X, Chen P, Yu Q, Chu H, Yang S, et al. Superior corrosion-resistant 3D porous magnetic graphene foam-ferrite nanocomposite with tunable electromagnetic wave absorption properties. Journal of Magnetism and Magnetic Materials 2019; 469: 428-436.

Yusoff AHM, Salimi MN, Gopinath SCB, Abdullah MMA, Samsudin EM. Catechin adsorption on magnetic hydroxyapatite nanoparticles: A synergistic interaction with calcium ions. Materials Chemistry and Physics 2020; 241: 122337.

Zhan X, Xiao L, Liang B. Removal of Pb(II) from Acid Mine Drainage with Bentonite-Steel Slag Composite Particles. Sustainability 2019; 11: 4476.

Zhang X, Li Y, Hou Y. Preparation of magnetic polyethylenimine lignin and its adsorption of Pb(II). Int J Biol Macromol 2019; 141: 1102-1110.